Advanced Fiber Materials
https://doi.org/10.1007/s42765-024-00484-8

RESEARCH ARTICLE

An Energy-Autonomous Wearable Fabric Powered by High-Power Density Sweat-Activated Batteries for Health Monitoring

Xiaoling Tong[1] · Tianjiao Hua[2] · Miaoyi Xu[1] · Dongzi Yang[2] · Gang Xiao[1,3] · Shuo Li[4] · Xiaohui Cao[5] · Yuanlong Shao[1,3,6]

Received: 17 July 2024 / Accepted: 30 August 2024
© Donghua University, Shanghai, China 2024

Abstract

The rapid advancement of personalized healthcare brings forth a myriad of self-powered integrated sweat fabric systems. However, challenges such as alkaline by-products, low open-circuit voltage and output power have made them unsuitable for the continuously powering biosensors. Here, we have designed a sweat-activated polyaniline/single-wall carbon nanotube||Zinc (PANI/SWCNTs||Zn) battery fabric featuring multiple redox states. This innovative battery achieves a high open-circuit voltage of 1.2 V within 1.0 s and boasts an impressive power density of 2.5 mW cm^{-2} due to the rapid solid–liquid two-phase electronic/ionic transfer interface. In-depth characterization reveals that the discharge mechanism involves the reduction of emeraldine salt to leucoemeraldine without oxygen reduction. By integrating this system seamlessly, the sweat-activated batteries can directly power a patterned light-emitting diode and a multiplexed sweat biosensor, while wirelessly transmitting data to a user interface via Bluetooth. This strategic design offers safety warnings and continuous real-time health monitoring for night walking or running. This work paves the way for the development of an efficient and sustainable energy-autonomous electronic fabric system tailored for individual health monitoring.

Keywords Sweat-activated battery · Self-powered · Integrated biosensor · Real-time sweat monitoring

1 Introduction

Smart fabric sensing systems often termed 'labs on textiles' for monitoring, recording, and feedback on various physiological and electrochemical signals related to human health [1–4]. Sweat fabric sensing systems equipped with electrochemical sensors can detect electrolytes, metabolites, nutrients, and drugs [5, 6]. High energy output is essential for actuating multiple sensors and enabling wireless data transmission during prolonged operation [7]. However, traditional power sources, such as commercial lithium polymer pouches, are bulky, rigid, and unsafe, leading to intermittent power supplies and reduced ergonomic comfort [8, 9].

Human sweat contains a wealth of chemicals that serve as biomarkers of health, offers a natural and biocompatible bioenergy source for powering fabric sensors [9–11]. Typically, enzymatic biofuel cells, convert sweat metabolite into electricity, but they face challenges due to their reliance on metabolites concentration like glucose or lactic acid, resulting in low and unstable energy supplies [12, 13]. Besides biofuel molecules, sweat contains abundant ions, such as Na^+, K^+, and Cl^-, which provide reliable electrolytes for wearable energy devices [14, 15]. Sweat-activated batteries,

✉ Yuanlong Shao
shaoyuanlong@pku.edu.cn

1 School of Materials Science and Engineering, Peking University, Beijing 100871, People's Republic of China

2 College of Energy, Soochow Institute for Energy and Materials Innovations (SIEMIS), Key Laboratory for Advanced Carbon Materials and Wearable Energy Technologies of Jiangsu Province, SUDA-BGI Collaborative Innovation Center, Soochow University, Suzhou 215006, People's Republic of China

3 Beijing Graphene Institute (BGI), Beijing 100095, People's Republic of China

4 Materials Science and Engineering, Physical Science and Engineering, King Abdullah University of Science and Technology (KAUST), 23955-6900 Thuwal, Saudi Arabia

5 State Key Laboratory for Modification of Chemical Fibers and Polymer Materials College of Materials Science and Engineering, Donghua University, Shanghai 201620, People's Republic of China

6 Academy for Advanced Interdisciplinary Studies, Peking University, Beijing 100871, People's Republic of China

Published online: 18 September 2024

such as metal-air batteries, have emerged with high energy density and output voltages of around 1 V [16, 17]. However, the hydroxide product at the cathode can cause metabolic alkalosis (Fig. S1a). Additionally, the solid–liquid–gas redox interface between the electrode/electrolyte interfaces leads to sluggish electron transfer or ion diffusion, resulting in inadequate power density and fluctuating energy supply. Therefore, a novel fibrous sweat-activated battery with high biocompatibility, energy, and power density is needed to meet the demands of sweat-sensing fabric.

Polyaniline (PANI) is an excellent candidate for biological electrode materials due to its biocompatibility and multiple redox states [leucoemeraldine (LEB)–emeraldine salt (ES)–emeraldine base (EB)–pernigraniline (PB)], which enables high energy density [18]. PANI preferentially forms a reduced state, which allows accelerated electron transfer and ion diffusion within the solid–liquid two-phase interface (Fig. S1b), leading to high-power density charge storage devices capable of powering electronics such as light-emitting diode (LED) and printed circuit boards (PCB). The long conjugate chain of PANI also facilitates the fabrication of high-modulus fibers due to the robust π-interactions. However, PANI fibers face challenges in mechanical strength and electronic conductivity due to long-range disorder in PANI polymer chains, which exacerbates structural defects, and impedes efficient charge transport [19–23]. Additionally, the limited electronic conductivity can severely degrade electrochemical performance [24]. Single-wall carbon nanotubes (SWCNTs) could serve as a rigid polymer chain to be triggered orientation by the fluid shear during the wet-spinning process due to their one-dimensional (1D) topology [25, 26]. It can induce the alignment of molecular chains along the SWCNT axis and increase the crystallization of the fibers, improving electronic conductivity and mechanical performance.

Herein, we present a strategy for fabricating SWCNT-reinforced PANI fibers via wet spinning method. The π–π interaction between SWCNTs and PANI triggers the alignment of PANI molecular chains along the SWCNTs axis (Fig. 1b). The resulting PANI/SWCNTs fibers were directly

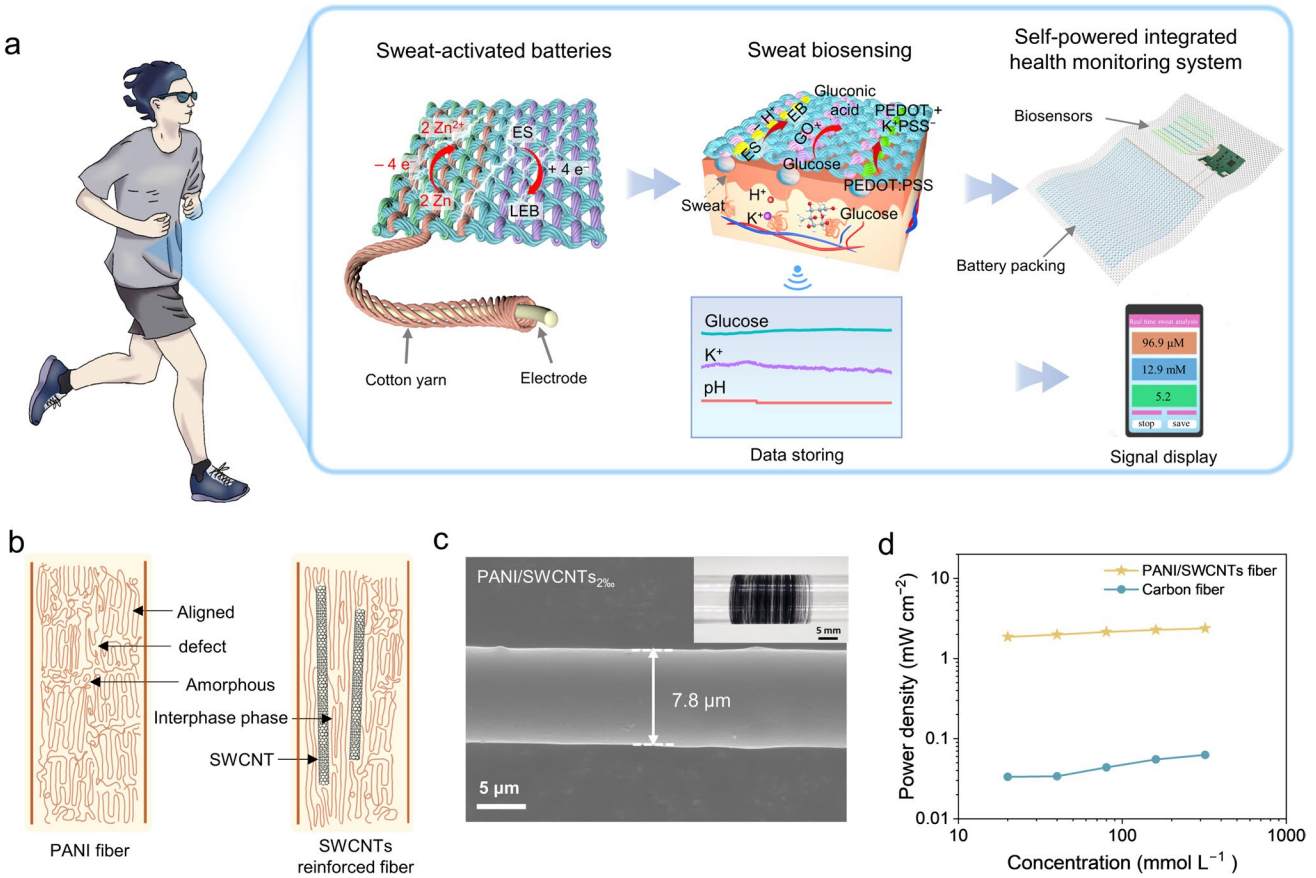

Fig. 1 Design and concept of the integrated self-powered biosensing system. **a** Schematic of a sweat-activated battery for energy supply, a PCB for signal transmission, and wirelessly transmitting data to a mobile user interface via Bluetooth. **b** The SWCNTs induced interphase between PANI and SWCNTs. **c** The surface morphology of ultrafine PANI/SWCNTs$_{2‰}$ fiber and its photograph with 70-m-long (inset). **d** The high-power density of PANI/SWCNTs||Zn fiber battery compared with carbon fiber||Zn battery in 20 mmol NaCl electrolyte with various concentrations

integrated into a wearable self-powered sweat-sensing fabric system. The sweat-activated PANI/SWCNTs||Zn battery enables continuous multiplexed monitoring of key metabolic biomarkers (e.g., pH, K^+, and glucose) and wirelessly transmits personalized bio-information to a user interface via Bluetooth (Fig. 1a). The sweat-activated battery comprises a PANI/SWCNTs cathode and a Zn wire anode, both wrapped in hydrophilic cotton yarn. The yarn acts as a separator and salt bridge, efficiently absorbing sweat and facilitating liquid transport through micro/nanosized channels via capillary forces. Continuous perspiration during exercise activates the battery generating electrical energy to power electronic systems. The PANI/SWCNTs||Zn battery operates by reducing PANI from ES to LEB while oxidizing Zn to Zn^{2+} (Fig. S1b), achieving a higher power density of over 1.8 mW cm^{-2} compared to 0.03–0.06 mW cm^{-2} for Zn-carbon fiber battery (Fig. 1d, Fig. S2). This electrochemical process minimally impacts the electrolyte pH, enabling the PANI/SWCNTs||Zn batteries to power multiplexed sensing and a PCB with wireless data transmission. This integrated self-powered biosensor system was successfully validated in vitro during human trials, underscoring its potential for developing self-powered electronic fabrics and advancing personalized healthcare.

2 Experimental Section

2.1 The Fabrication of Ultrafine PANI/SWCNTs Fibers

PANI powder (Aladdin, 98%, 25233-30-1) was doped by camphor sulfonic acid (CSA, Aladdin, 99%, 35963-20-3) through ball-milling for 2 h with a molar ratio of 2:1. The doped PANI/CSA powder was dissolved in m-cresol at a concentration of 100 mg mL^{-1}. The SWCNTs (XFNANO, 95%, XFS19) powder was dispersed in m-cresol (1 mg mL^{-1}) and ultrasonic for 30 min. Afterward, the PANI and SWCNTs dispersions were mixed in the needed proportion and then the m-cresol was added to the mixed dispersion to guarantee the total volume consistency. The dispersion was stirred above 12 h to obtain a uniform and viscous spinning dope, subsequently extruded into a dimethyl formamide coagulation bath with 70 cm length through a PEEK microtube of 32 G (inner diameter is 100 μm) at a spinning rate of 1 mL min^{-1}. The PANI/SWCNTs fibers were rapidly drawn out from the coagulation bath with a draw ratio of $\lambda = 2.2$ and collected continuously at room temperature.

2.2 Preparation of Biosensing Electrodes

Preparation of pH-sensing fibers: The PANI/SWCNTs$_{2‰}$ fibers were directly applied as the pH-sensing electrodes.

Preparation of glucose-sensing fibers: Platinum (Pt) nanoparticles were deposited on the PANI/SWCNTs$_{2‰}$ fibers by electrochemical deposition in 1 mmol L^{-1} potassium chloroplatinate (K_2PtCl_6) and 100 mmol L^{-1} potassium chloride (KCl) mixed solution at 0.5 V for 10 s, − 0.7 V for 10 s with 50 cycles to improve the sensitivity of the glucose-sensing fiber [27]. Chitosan solution (1.0 wt%) was prepared by dissolving 10 mg chitosan into 1% acetic acid with continuous magnetic stirring for 30 min. SWCNTs were subsequently added to the chitosan solution at a concentration of 2 mg mL^{-1}. Afterward, glucose oxidase (40 mg mL^{-1}) was added into the mixture solution by continuous stirring and ultrasonic treatment for 30 min to form a uniform and viscous mixed solution. Finally, 4 μL mixture solution was dipped onto the PANI/SWCNTs$_{2‰}$ fibers and dried overnight at 4 °C to obtain the glucose-sensing biosensing electrodes.

Preparation of K^+-sensing fibers: Poly(3,4-ethylenedioxythiophene) poly(styrenesulfonate) (PEDOT:PSS) was first deposited onto the PANI/SWCNTs$_{2‰}$ fibers by electrochemical polymerization in a 0.01 M 3,4-ethylenedioxythiophene (EDOT) and 0.1 M sodium poly(styrenesulfonate) (NaPSS) mixture solution. Then, the K^+-selective membrane precursor was prepared by dissolving 0.50 mg sodium tetraphenylborate (NaTPB), 32.75 mg high-molecular weight polyvinyl chloride (PVC), 64.75 mg bis(2-ethylehexyl) sebacate (DOS) and 2.0 mg potassium ionophore in 350 μL cyclohexanone. Such a precursor solution was dipped onto the PANI/SWCNTs$_{2‰}$ fibers and dried at 4 °C overnight to obtain the K^+-selective biosensing electrodes.

All the biosensing electrodes are about 2 cm. The reproducibility of the sensors was investigated by four samples, which were fabricated in different batches.

2.3 Fabrication of Sweat-Activated Batteries.

First, the cotton yarn was cleaned with 10 g mL^{-1} sodium bicarbonate ($NaHCO_3$) solution at 100 °C for 10 min and then washed with deionized water several times. After drying, the cotton yarn was hydrophilic. Afterward, PANI/SWCNTs$_{2‰}$ fiber anode and Zn wire cathode were inserted into cotton yarn and then encapsulated into a polyvinyl chloride tube. The sodium chloride (NaCl) electrolyte was injected into the tube to obtain the fiber-shaped sweat-activated batteries.

2.4 Textile Woven Sweat-Activated Batteries

A simple weaving machine was employed to weave the fiber electrode into a plain-structured fabric, in which the cathodes and anodes were utilized as weft. The number of integrated batteries could be adjusted. The melted wax was dropped onto the cotton yarn and cooled down at room

temperature for 10 min to obtain a hydrophobic barrier between two neighbored batteries.

2.5 Cytotoxicity Analysis

The animal experiment has been approved by the animal ethical and welfare committee. Approval No. YSY-DWLL-2024304. Cell viability was tested on B16-F0 cells (Mouse melanoma cells). B16-F0 cells were cultured in Dulbecco's modified Eagle's medium (DMEH-214.5g/Liter Glucose) with 10% FBS. Cells were seeded on Dulbecco's modified eagle medium (DMEM) with PANI/SWCNTs$_{2‰}$. The DMEM culture with and without cells was used as a positive and blank control, respectively. 200 μL of staining solution for each condition was transferred into ELISA (enzyme-linked immunosorbent assay, Synergy2 SLFPTAD, USA, BioTek Instruments, Inc.) for spectrophotometric microscopy (U-LH100HGAPO, Japan, Olympus corporation). The absorbance of the solutions was measured spectrophotometrically at 450 nm.

2.6 Physicochemical Characterization

A Hitachi SU8010 scanning electron microscope (SEM) was employed to characterize the surface and cross-section microstructures of PANI/SWCNTs fibers. A probe station (Lakeshore CRX-6.5K) was employed to assess the electronic conductivity. Dynamometer (Instron 5969, 5 N) was utilized to calculate the mechanical performance of the fibers. X-ray diffraction (Bruker D8 Advance Diffractometer) with Cu-Kα radiation ($\lambda = 1.5406$ Å) was applied to characterize the crystal structure at a scan rate of 1° min^{-1}. The *I–V* curves were used to characterize the electronic conductivity of the fibers on a micromanipulator probe station integrated with a semiconductor analyzer (Keithley 4200 SCS). The electronic conductivity (σ) of fibers was defined as Eq. (1).

$$\sigma = \frac{l}{R \times A}, \tag{1}$$

where l refers to the length between the two conductive Ag paste, R is the resistance, A is the cross-sectional area of the fiber. The corresponding schematic of a two-electrode measurement was illustrated in Fig. S3.

2.7 Ex situ Characterization

Ex situ electrochemical characterization was carried out by line scan voltammetry (LSV) at a scan rate of 1 mV s^{-1} to a settled potential of 1.2, 0.75, and 0.25 V during the discharging process with a delay time of 600 s. To elucidate the discharge mechanism of the sweat-activated PANI/SWCNTs||Zn batteries without external disturbance, the pure PANI fibers were employed and discharged to the preset potentials and then washed with ultrapure water and vacuum dried at 40 °C before the ex situ FTIR and Raman measurement. All the measurements were repeated at least three times and possessed reproducibility.

2.8 Computation Fluid Dynamics Simulations

Viscometer (Ranhui LVT-1, Shanghai) was employed to characterize the rheological behavior. The non-Newtonian flow behavior was calculated by the power-law viscosity model according to Eq. (2).

$$\eta = K\dot{\gamma}^{n-1}, \tag{2}$$

where η is the apparent viscosity, $\dot{\gamma}$ is the shear rate, K is an empirical constant, and n is the non-Newtonian index.

2.9 Characterization of the Sweating Rate

Three sheets of 3 cm × 3 cm absorbent patch (medical gauze + sportswear fabric + sealing tape) were taped to different positions on the body. The mass variation after the different times (Δm) was tested. The sweating rate was calculated by Eq. (3) as follows:

$$\text{Sweating rate} = \frac{\Delta m}{t \times A \times \rho}, \tag{3}$$

where t, A, and ρ refer to the test time, area of the absorbent patch, and density of sweat, respectively.

The performance of each sweat-activated battery was characterized by both LSV and constant discharge in a two-electrode system. The power of the batteries was calculated by Eq. (4).

$$P = V \times I, \tag{4}$$

where P, V, and I refer to the power, potential and current.

2.10 On-Body Sweat Analysis

A female subject aged from 30 years old was recruited from Peking University and gave written, informed consent before participating in the study. The PANI/SWCNTs$_{2‰}$-based sensing fibers were woven into a piece of gauze, which was integrated with a PCB and a piece of sweat-activated battery textile, further equipped into a T-shirt. The in situ continuous sweat analysis was conducted by a subject wearing the garment device and walking or running. The sensing analysis results were recorded directly on the smartphone via a customized application.

3 Results and Discussion

3.1 Second-Order Heading Continuous Preparation via Wet-Spinning and Physical Characterization of PANI/SWCNTs Fibers

Figure 2a schematically illustrates the role of SWCNTs in enhancing the orientation of PANI chains during a wet-spinning process. Firstly, the π–π interaction between SWCNTs and PANI promotes the formation of an interphase polymer layer, which induces the alignment of PANI molecular chains along the SWCNT axis [28]. Secondly, the fluid-induced shear force during spinning further aligns the SWCNTs along the flow direction, especially as the spinning dope passes through the narrow spinneret. This alignment further orients the PANI chains along the SWCNT surface, intensifying the orderly packing of PANI molecules and enhancing orientation and crystallinity within a certain range. Thirdly, the irregular PANI molecules beyond the interface are aligned through rapid stretching in a coagulation bath, resulting in ultrafine, smooth fibers with a diameter of 7.8 μm (Fig. 1c). This rapid stretching also enables high production efficiency, exceeding 10 m min^{-1} for PANI/SWCNTs fibers. As shown in the inset of Fig. 1c, 70-m-long ultrafine PANI/SWCNTs fibers have been successfully produced.

Rheological properties are critical in determining the spinnability of a wet-spinning dope and the physicochemical characteristics of the resulting fibers [29]. The PANI/SWCNT dopes with various SWCNT ratios of 0, 0.5, 1, 2, 5, and 10‰ have been prepared for further analysis. As summarized in Fig. S4g-j, SWCNTs are uniformly. The SWCNTs strengthen the intertwining interactions between PANI and SWCNTs chains, leading to a gradual increase in shear viscosity from 29.5 kPa s (PANI) to 69.6 kPa s (PANI/$SWCNTs_{2‰}$) (Fig. 5a, Fig. S4a-d). However, with further increase in SWCNT content to 10‰, the viscosity decreases

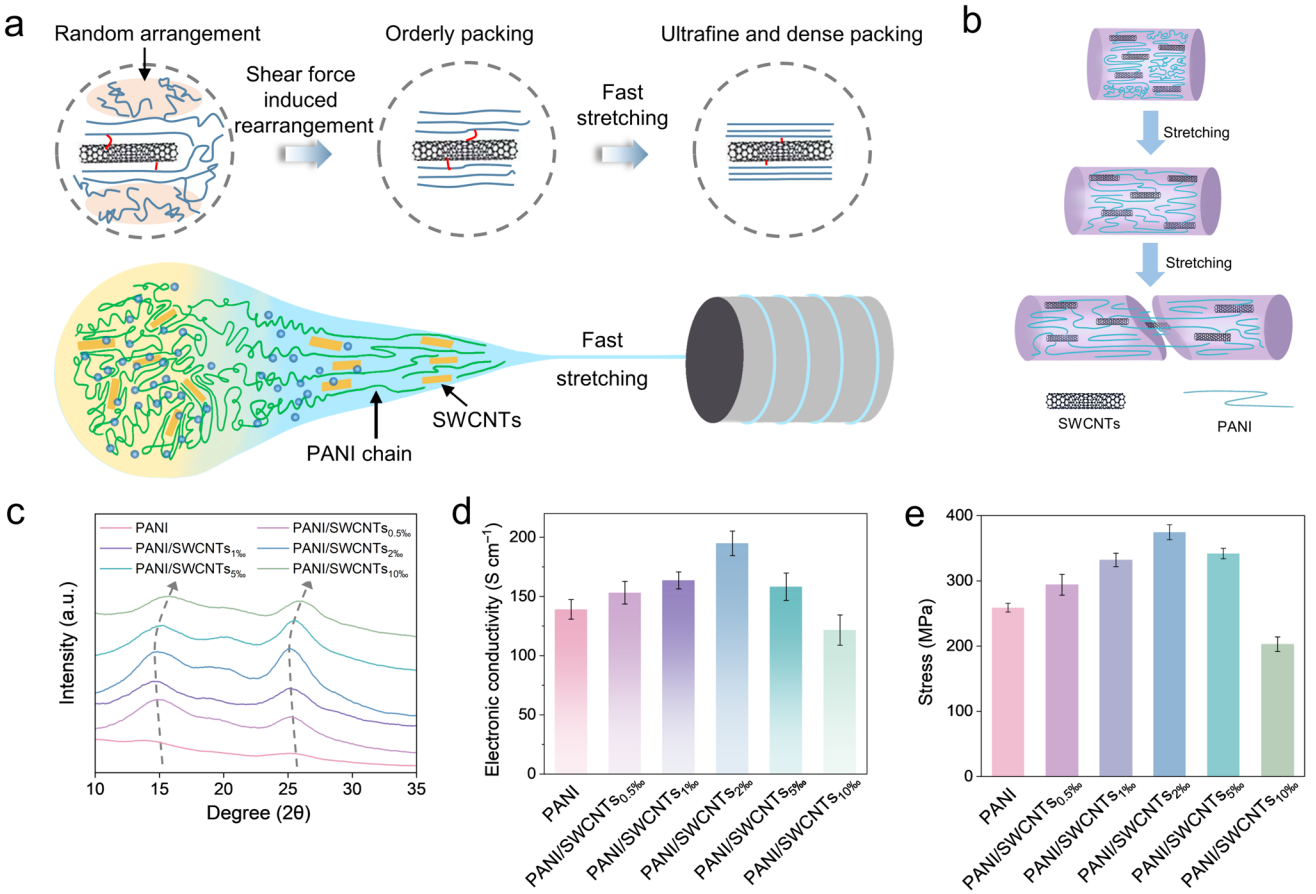

Fig. 2 Continuous preparation of ultrafine PANI/SWCNTs fibers. **a** Schematic illustration of the PANI/S WCNTs wet-spinning process. The magnified graphic highlights the SWCNTs and fast stretching-induced rearrangement of PANI molecules along the SWCNTs' axial direction during the wet-spinning process. **b** The enhanced interface stress of the PANI/SWCNTs fibers under tension. **c** XRD patterns of the PANI/SWCNTs fibers with different SWCNTs mass ratios. **d** The electronic conductivity. **e** Mechanical performance of the PANI/SWCNTs fibers with different mass ratios

to 52.5 kPa, may be due to the undesirable agglomeration of SWCNT bundles in the m-cresol solvent (Fig. S5a, Fig. S4e,f, Fig. S4k,l), which disrupts the interface interaction between PANI and SWCNTs. The non-Newtonian index (n) is another crucial factor for evaluating the spinnability of a wet-spinning dope. All PANI/SWCNTs dopes exhibit pseudoplastic shear-thinning behavior, which is ideal for wet spinning. The optimal n of −0.64 for the PANI/SWCNTs$_{2‰}$ dope, suggests it is most suitable for further spinning (Fig. S5b). These findings further supported by Fig. S6a–f, which shows that fibers can be directly formed by pulling the PANI/SWCNTs spinning dope with various SWCNT contents.

Fig. S6 and Fig. S7 display the top-surface and magnified cross-sectional SEM images of PANI/SWCNTs fibers with varying SWCNT mass ratios from 0 to 10‰. As the SWCNT content increased to 2‰, the fiber diameters slightly expanded from 6.0 to 7.8 μm (Fig. S6a-d). However, more pronounced increase in diameter was observed when the SWCNT content reached 10‰, likely due to decreased viscoelasticity, which adversely impacted the drafting effect during the wet-spinning process (Fig. S6e,f). The appropriate viscoelasticity of the PANI/SWCNTs$_{2‰}$ spinning dope produced fibers with smooth surfaces (Fig. S6d) and densely packed cross-sectional morphologies (Fig. S7d). In contrast, pure PANI fibers exhibits significant aggregation (Fig. S7a). The introduction of SWCNTs improved the PANI dispersion through enhanced π-π interactions at the PANI/SWCNT interface, resulting in a uniform cross-sectional morphology (Fig. S7b-d). However, excessive SWCNTs lead to aggregation, introducing defects in the PANI/SWCNTs$_{10‰}$ fibers (Fig. S7e, f).

To further investigate the enhanced interactions between the PANI and SWCNT interfaces, structural variations in the spinning dopes with varying SWCNT content were analyzed using FTIR (Fig. S8a). The peaks at 1574, 1493, 1298, and 1134 cm^{-1} correspond to C–H quinonoid ring (Q) stretching, C–N benzenoid ring (B) stretching, C–N stretching of secondary aromatic amines, and the stretching vibration of –NH$^+$ = (in the B–NH$^+$ = Q segment), respectively [30–33]. For PANI/SWCNTs$_{2‰}$, the C − H (Q)/C–N (B) and –NH$^+$ = (B–NH$^+$ = Q segment)/C–N (B) peak ratios increased to 1.18 and 0.93, respectively, indicating a stronger π–π interaction between the PANI and SWCNT interfaces (Table S1). This enhanced interaction resulted in an optimal electronic conductivity of 194.9 S cm^{-1}, outperforming the conductivities of 139.1, 153.2, 163.6, 158.3, and 121.6 S cm^{-1} for PANI, PANI/SWCNTs$_{0.5‰}$, PANI/SWCNTs$_{1‰}$, PANI/SWCNTs$_{5‰}$, and PANI/SWCNTs$_{10‰}$, respectively (Fig. 2d). Figure 2b schematically illustrates the improved interface between PANI and SWCNTs, which enhances load transfer efficiency (Fig. S9). As shown in Fig. 2e and Fig. S10, the PANI/SWCNTs$_{2‰}$ fiber achieved a maximum stress of 374.4 MPa, representing a 44.7% increase over pure PANI (258.7 MPa). However, further increases in SWCNT content leads to a decline in mechanical stress, eventually falling below the stress levels of pure PANI fibers. The reduction in electronic conductivity and mechanical property is ascribed to the SWCNT aggregation and the resulting defects (Fig. S7e,f).

3.2 Electrochemical Performance Characterization of Sweat Activated PANI/SWCNTs||Zn Batteries

The ultrafine morphology of PANI/SWCNTs fibers provides optimized electroactive surfaces, leading to excellent energy capacities. To assess the electrochemical performance of PANI/SWCNTs fibers, we assembled a yarn battery in a parallel core-sheath configuration. As schematically illustrated in Fig. S11, the battery comprises a PANI/SWCNTs$_{2‰}$ fiber cathode and a Zn wire anode, each wrapped separately in hydrophilic cotton sheaths. The yarn acts as both a separator and a micro-reservoir for sweat capture and collection, containing numerous micro/nanosized channels that enhance electrolyte infiltration through capillary forces (Fig. S12 and Fig. S13). Given that Na^+ and Cl^- are the primary components in sweat, an 80 mmol L^{-1} NaCl electrolyte was used to simulate human sweat and activate the PANI/SWCNTs||Zn batteries. As shown in Fig. 3b, only 10 μL of NaCl solution is needed to activate the battery, resulting in a sharp increase in open-circuit voltage (OCV) to 1.16 V within 1.1 s. The voltage stabilizes plateau at 1.2 V with the addition of another 10 μL of sweat solution. The discharge capacities of PANI/SWCNTs fiber batteries have been evaluated using a galvanostatic charge/discharge technique. As depicted in the inset of Fig. 3b, the battery exhibits a high discharge plateau at 1.07 V and maintains discharge for 7.1 h at a constant current of 0.02 mA cm^{-2}. The corresponding discharge capacity and power density are 0.14 mAh cm^{-2} and 2.10 mW cm^{-2}, respectively. To ensure the biocompatibility of the battery, the cytotoxicity of PANI/SWCNTs fibers was assessed by measuring the viability of B16-F0 cells cultured on the surface of PANI/SWCNTs$_{2‰}$ fibers in DMEM after 48 h. As shown in Fig. S14, the cell viability test conforms the good biocompatibility of the PANI/SWCNTs$_{2‰}$ fibers.

Given the variable concentration of sweat, discharge performances were further evaluated at different NaCl concentrations ranging from 20 to 320 mmol L^{-1} (Fig. 3c and Fig. S15). A high-power density of 2.49 mW cm^{-2} was achieved in 320 mmol L^{-1} NaCl, while maintaining a strong capacity retention of 1.79 mW cm^{-2} even at 20 mmol L^{-1} NaCl. The high open-circuit voltage and power density of the resulting PANI/SWCNTs||Zn fiber battery (Fig. 3d) surpass those of most previously reported self-powered metal-air [16, 17, 34–37] and biofuel batteries (Table S2) [3, 12, 13, 38–42].

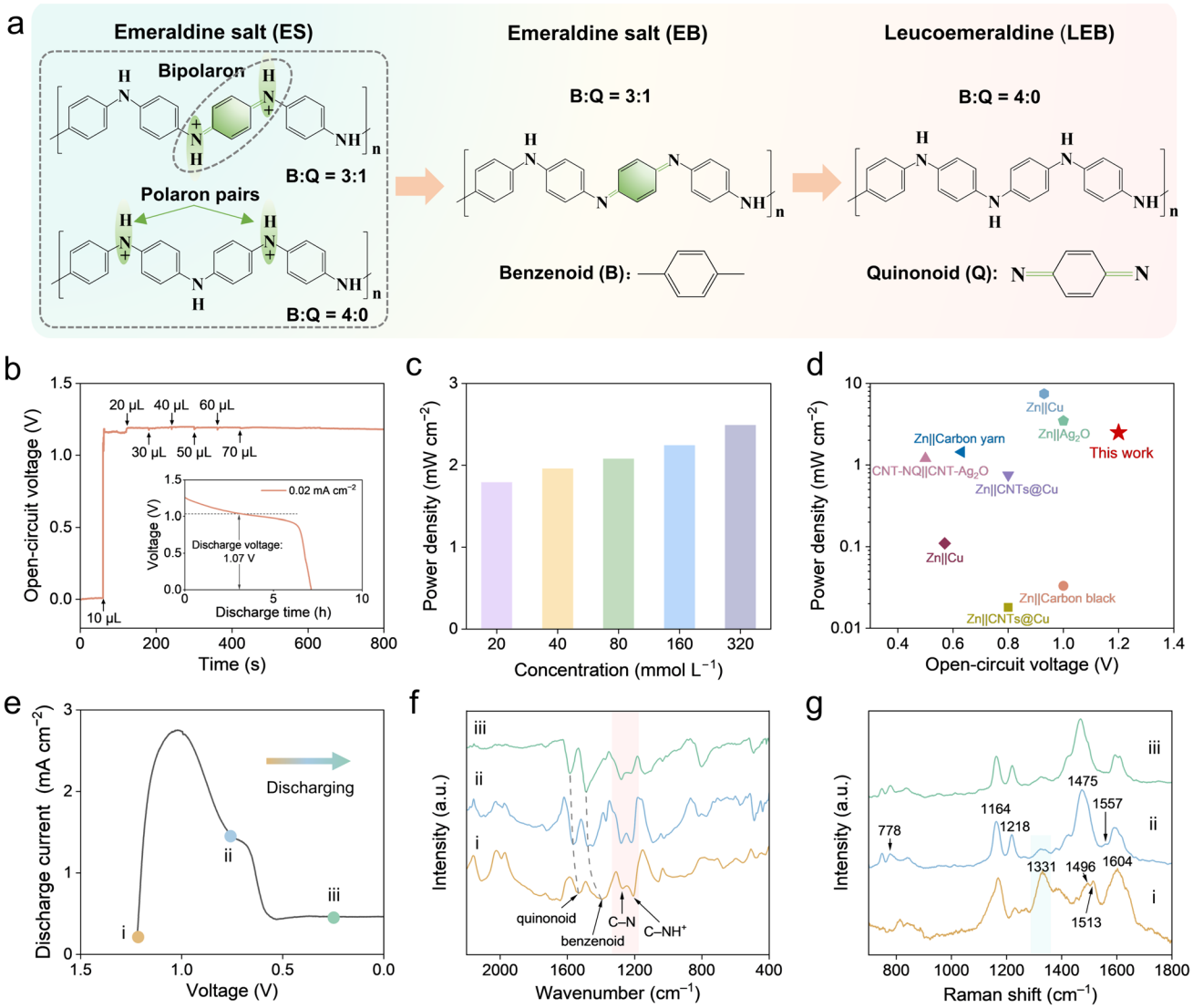

Fig. 3 Electrochemical mechanism and performance characterizations of the PANI/SWCNTs$_{2‰}$||Zn batteries in NaCl electrolytes. **a** Schematic illustration of the discharge mechanism of PANI with reduction reaction. **b** The open-circuit voltage of the batteries in response to a continuously increased NaCl solution (80 mmol L^{-1}). Inset: galvanostatic discharge curves of the battery at a current density of 0.02 mA cm^{-2}. **c** Power density of the batteries in NaCl electrolyte with concentrations ranging from 20 to 320 mmol L^{-1}. **d** The comparison of open-circuit voltage and power density between this work and other reported sweat-activated batteries. **e** Ex situ electrochemical characterization by LSV at a scan rate of 2 mV s^{-1} to a preset potential during the discharging process. **f** FTIR and **g** Raman spectra of PANI fibers at different electrochemical steps

3.3 Electrochemical Mechanism of Sweat Activated PANI/SWCNTs||Zn Batteries

To elucidate the mechanism behind the superior power density of PANI/SWCNTs||Zn fiber batteries, Fig. 3e presents the line scan voltammetry (LSV) curve at a sweep rate of 2 mV s^{-1} within a potential range from OCV (i) to 0.25 V (iii) vs. Ag/AgCl. During the initial discharge stage, a discernible reduction peak around 1.02 V contributes to the high discharge capacity of the PANI/SWCNTs, followed by a secondary peak around 0.68 V. Notably, the discharge current drops to zero as the voltage decreases below 0.5 V, with no polarization phenomenon observed, indicating that the discharge process avoids oxygen reduction.

The chemical structural evolution during the electrochemical discharge process was systematically investigated using a series of ex situ characterization techniques. As depicted in Fig. 3f, ex situ FTIR spectra have been applied to track molecular evolution. Peaks centered at 1209 and 1273 can be assigned to C–NH^+ stretching (characteristic of the polaron form of PANI emeraldine salt) and C–N stretching of secondary aromatic amines, respectively [31, 32, 43].

This indicates a progressively decrease in C–NH^+ and an increase in C – N until discharge reaches to 0.83 V (ii), suggesting that the emeraldine salt (ES) with polaron pairs or bipolar are transforming into emeraldine base (EB). Additionally, an intensified quinonoid (Q) ring peak at 1531 cm^{-1} corresponds to Q ring stretching, indicating the transformation of polaron pairs into bipolar or further development into EB. Upon further discharge to 0.25 V (iii), attenuation of Q and the enhancement of benzenoid (B) indicate that EB has been reduced to the leucoemeraldine state (LEB). Consequently, bipolar and polar coexist in PANI during the discharge process.

Ex situ Raman spectroscopy (Fig. 3g) was also employed to characterize the PANI structural evolution of PANI during discharge. Upon discharging to 0.83 V, the peak at 1331 cm^{-1} (C–N^+) dramatically decreases significantly, while the peaks corresponding to C–N stretching vibrations of EB and Q deformation at 1218 and 778 cm^{-1} increase [30, 44]. Furthermore, the N–H bending (semiquinone) and C = N stretching vibrations in Q centered at 1513 and 1496 cm^{-1} disappear, and a new peak appears at 1475 cm^{-1}, suggesting that the polaron pairs or bipolar of ES dedoped into (EB) at 0.83 V. Moreover, the peak at 1604 cm^{-1}, corresponding to C–C stretching of the para-distributed B ring substantially decreases, while the C=N stretching and C=C stretching vibrations of Q at 1557 cm^{-1} and 1475 cm^{-1} increase significantly [43]. The EB form of PANI contains a higher imine/amine and Q/B ratio than the ES form, indicating that ES is reduced to EB as the PANI discharges from 1.22 to 0.83 V. In summary, PANI (ES) with polaron pairs or bipolar is preferentially reduced to EB and further reduced to the LEB state (Fig. 3a).

To meet the various power output demands, discharge performances were evaluated at different current densities ranging from 0.1 to 1 mA cm^{-2} (Fig. S16a,b), displaying only marginal capacity deterioration from 0.14 to 0.12 mAh cm^{-2}, and demonstrating superior rate performance with a capacity retention of 85.7%. Multiple PANI/SWCNTs||Zn batteries were connected in series or parallel to expand the output voltage and power. As the number of connected batteries increased from 1 to 4, the OCV of the in-series battery packs increase from 1.26 to 4.83 V (Fig. S17a and inset). The battery pack successfully powered a red LED with a minimum driving voltage of 2.0 V (Fig. S18). Similarly, the power density of the parallel-connected battery pack increased linearly from 2.08 to 8.54 mW cm^{-2} (Fig. S17b, c). In addition, this high-power density also enabled a high current tolerance, charging a supercapacitor to over 1.1 V in just 1.0 s and maintaining stability after 5.4 s (Fig. S19a, b). The self-powered supercapacitor can be continuously charged and discharged at different currents (Fig. S19c). Additionally, the 1D fiber battery exhibits excellent flexibility, enduring repeated bending at a frequency of 0.5 Hz with a curvature radius of 4.7 mm (Fig. S20 and inset). The assembled PANI/SWCNTs||Zn fibrous battery withstands up to 5000 bending cycles without significant fluctuation in output voltage. Upon cessation of bending, the output voltage immediately returns to its original level. These results demonstrate that the PANI/SWCNTs||Zn battery can be sweat-activated while maintaining excellent mechanical and electrochemical stability.

3.4 Bio-sensing Properties of PANI/SWCNTs Fibers in Physiological Environment

Benefitting from the 1D flexible structure, the PANI/SWCNTs fiber-based biosensor electrodes can be easily woven into fabrics to assess various biomarkers in human sweat (Fig. 4a and Fig. S21). The intrinsic proton doping and dedoping properties of PANI provide high pH responsiveness [45]. According to the Nernst equation, the potential change is proportional to the logarithm of the H^+ concentration, as the H^+ concentrations reach equilibrium between the electrode and solution. Figure 4b and Fig. S22a display the open-circuit potential in an electrolyte with pH ranging from 4.0 to 7.0, corresponding to the human sweat pH levels. This pH biosensor exhibits near-Nernstian behavior with high sensitivity of (62.1 ± 1.5) mV pH^{-1} and excellent linearity (R^2 = 0.996 ± 0.002), comparable to state-of-the-art pH sensors. For an individual, the pH fluctuates slightly during continuous exercise. The PANI/SWCNTs electrode shows high reproducibility (Fig. 4b and Fig. S22a inset) and reversibility with minimal potential drift (Fig. S22c). Additionally, this pH sensor demonstrates excellent precision within the pH range of 4.5–5.5 (Fig. 4c). The long-term stability of this pH-sensing electrode has also been confirmed (Fig. 4d).

Given the variability of physiological environments, anti-interference capability is crucial for sweat biosensors, especially considering the diverse climate and metabolites that can affect sensing stability. Thus, the stability of the pH sensing electrode has been evaluated by introducing interfering ions and metabolites into the target electrolyte solution, which contained 100 mmol L^{-1} NaCl, 16 mmol L^{-1} potassium chloride (KCl), 300 µmol L^{-1} glucose, 50 mmol L^{-1} lactic acid (LA), 100 µmol L^{-1} uric acid (UA), and 100 µmol L^{-1} ascorbic acid (AA) (Fig. S22b). The negligible potential drift observed indicates excellent anti-interference performance in complex physiological environments.

To construct a glucose sensing electrode, PANI/SWCNTs fiber were first electrodeposited with Pt nanoparticles and then uniformly coated with glucose oxidase to enhance the sensitivity. In the analyte solution, glucose molecules are oxidized by glucose oxidase on the fiber surface, generating electrons. As shown in Fig. 4e, the current response to glucose concentrations ranging from 0 to 300 µmol L^{-1}, demonstrating a linear relationship

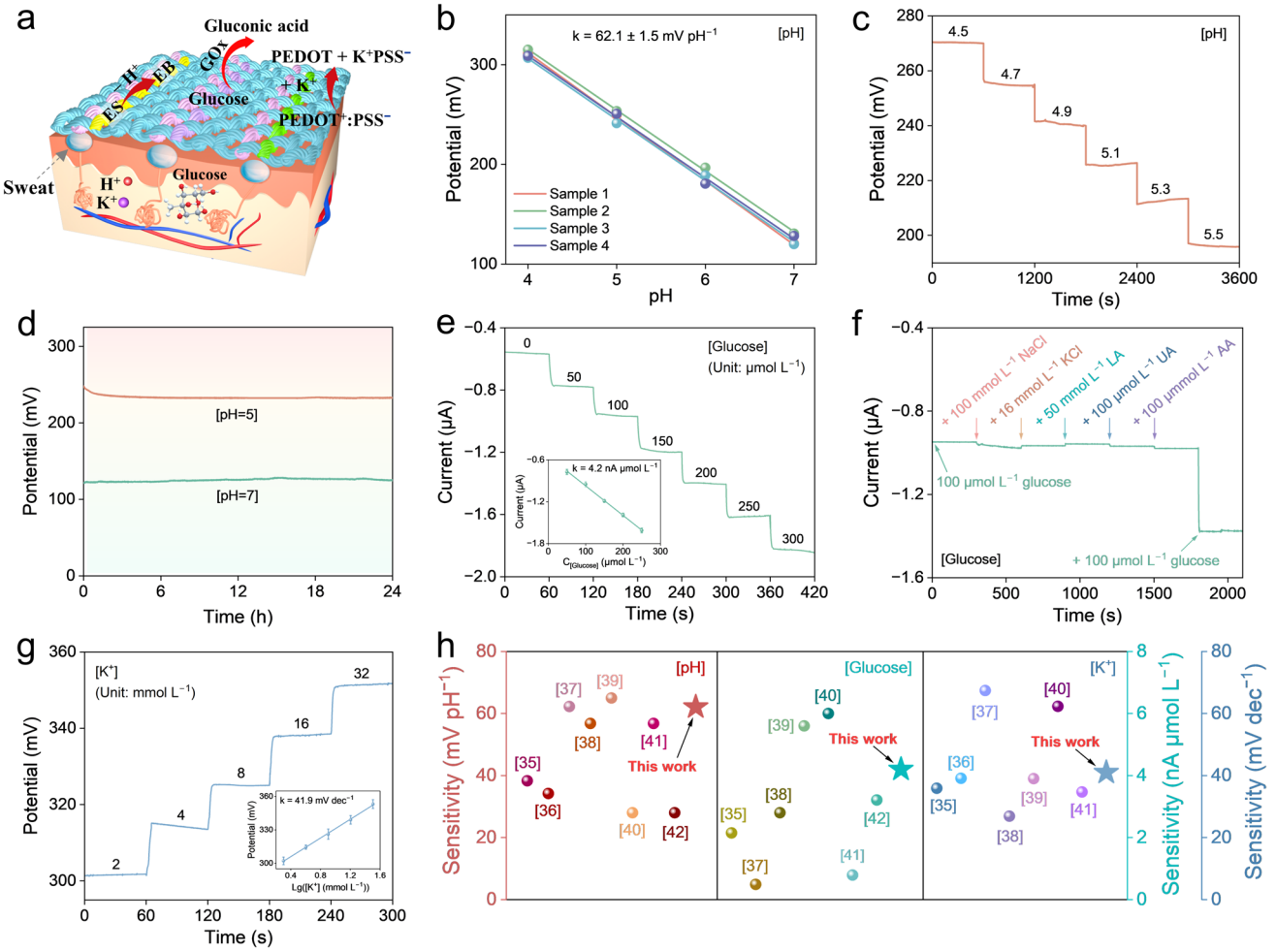

Fig. 4 The biosensing performance of PANI/SWCNTs$_{2‰}$ fiber-based electrode. **a** Schematic illustration of the pH, K^+, and glucose fiber sensor in sweat. **b** The reproducibility plots of the PANI/SWCNTs$_{2‰}$ fiber electrode to pH 4–7. **c** The high sensitivity of the pH electrode responds to pH 4.5–5.5. **d** Long-term stability of the pH sensing electrodes in pH 5 and 7 solutions. **e** Chronoamperometry responses and sensitivity plots (inset image) of the PANI/SWCNTs$_{2‰}$ fiber-based glucose electrode in 0–300 μmol L^{-1}. **f** The interference study of the PANI/SWCNTs$_{2‰}$ fiber-based glucose electrode. **g** Open-circuit potential responses and sensitivity plots (inset image) with a K^+ concentrations ranging from 2 to 32 mmol L^{-1}. **h** Sensitivity comparison of thus-fabricated pH, glucose, and K^+ sensing electrodes with other reported sensors

with a sensitivity of (4.2 ± 0.03) nA μmol L^{-1}. For the K^+ sensing electrode, a PEDOT:PSS layer and ion-selective membrane were electrochemically deposited. The ion-selective membrane screens the target ions, while the PEDOT:PSS layer acts as an ion–electron converter, altering the potential as the ion concentration changes. As shown in Fig. 4g, the K^+ sensing electrode displays excellent sensitivity of (41.9 ± 0.7) mV dec^{-1} across a concentration range of 2–32 mmol L^{-1} K^+. Both the glucose and K^+ sensing electrodes demonstrate great reproducibility (Fig. S23a, Fig. S24a), long-term stability (Fig. S23b, Fig. S24b), and strong anti-interference ability (Fig. 4f, Fig. S24c). The sensitivities of the pH, glucose, and K^+ biosensor electrodes surpass those of most patch or fiber sensors (Fig. 4h, Table S3) [27, 42, 46–53]. Additionally, the fabricated biosensor displays great stability before and after washing, indicating great reusability (Fig. S25).

3.5 Fabrication of PANI/SWCNTs Fiber Integrated Textile Patch for On-Body Sweat Analysis

The 1D design of PANI/SWCNTs||Zn batteries allows facile integration into fabrics, making them durable enough to provide sufficient electricity to power miniaturized electronic devices. These batteries can be integrated with a PCB containing an embedded chip and biosensor for real-time health monitoring (Fig. 5a, b). The integrated chip processes and transmits sensing signals to a Bluetooth-enabled mobile device with a user-friendly interface for displaying, storing, and exporting data. Given the ultrafine morphology of single

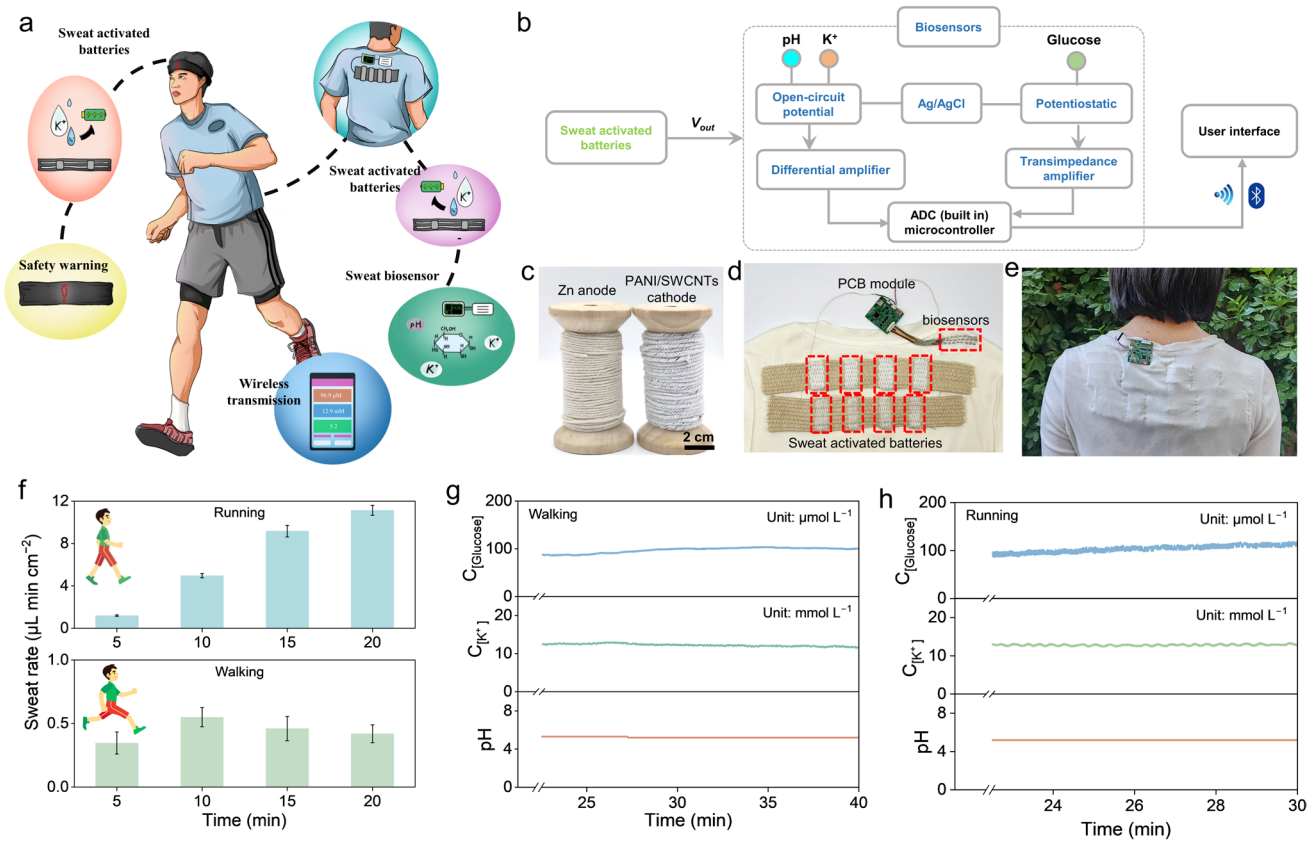

Fig. 5 The integrated self-powered integrated biosensor system for sweat monitoring. **a** Schematic illustrating the self-powered integrated biosensor system that integrates sweat-activated batteries, signal processing, sweat biosensing (pH, K^+, glucose), and Bluetooth-based wireless data transmitting to a user interface for real-time health monitoring. **b** System-level block diagram of the integrated self-powered sensing system illustrating the signal processing and transmission from PANI/SWCNTs-based bioelectrode to the Bluetooth-enabled mobile phone. **c** Photographs of the PANI/SWCNTs fibers were woven into yarns. **d** Sweat-activated batteries integrated with PCB module and biosensor, which were sewed into a shirt. **e** On-body demonstration of self-powered biosensor after exercise. **f** The sweat rate of an adult during walking and running. Real-time sweat pH, K^+, and glucose levels were obtained during constant walking **g** and running **h**

PANI/SWCNTs fiber with limited mass loading, a spindle of twisted PANI/SWCNTs fibers was woven into a cotton yarn to amplify the output power of a single battery (Fig. 5c and Fig. S26). This configuration delivers a high capacity of approximately 1.0 mAh at a discharge current of 1 mA and a peak power of 11.9 mW (Fig. S27). As displayed in Fig. S28a,c, three sweat-activated fiber batteries connected in series and four in parallel are sufficient to power 9 LEDs, functioning as safety warning lights for night walking or running. The LED lighting process is documented in Supplementary Video S1. Additionally, the fibrous electrode can be woven into fabrics (Fig. S29). Four in-series PANI/SWCNTs||Zn batteries were applied to weave a sweat-activated self-powered energy fabric, in which four strings of series-connected batteries were connected in parallel to form a battery pack. Due to the woven structure, the resulting energy fabric exhibits excellent mechanical flexibility. As shown in Fig. S30, after absorbing the NaCl solution, two self-powered energy fabrics could power a PCB (Video S2) and continuously monitor artificial sweat information while being bent or twisted, demonstrating high stability on curved surfaces. To showcase on-body analysis, a volunteer wore a shirt equipped with the biosensor system (Fig. 5e). The sweat rate is 0.4–0.6 μL min cm^{-2} during walking and 5.0–11.1 μL min cm^{-2} during running (Fig. 5f). Once sweat permeates the fabric, the multiplexed biosensor begins monitoring pH, K^+, and glucose levels in real-time. Figure 5g, h illustrates the integrated self-powered biosensor system's ability to collect signals of pH, K^+, and glucose concentrations. The biosensor signals fluctuate slightly at low-sweat rates (such as during walking) compared to high-sweat rates (such as during running). The pH and K^+ concentrations remain stable at 5.3 and 11.7–12.9 μmol L^{-1} during both walking and long-term running trials, respectively. Notably, glucose concentrations gradually increase, indicating continuous glucose loss in the subjects. Supplementary Video

S3 demonstrates the entire process of monitoring these signals, showcasing the feasibility of this integrated biosensor system.

4 Conclusions

In summary, we have developed innovative self-powered biosensor fabrics that integrate sweat-activated PANI/SWCNTs||Zn batteries with PANI/SWCNTs-based bioelectrodes for energy-autonomous and stable sensing. These PANI/SWCNTs||Zn batteries can be activated by sweat within 1.1 s, delivering a high output voltage of 1.2 V and a power density of 2.5 mW cm^{-2}. Notably, ex situ instrumental characterizations have elucidated the discharge mechanism of the PANI||Zn batteries, revealing a rapid solid–solid two-phase redox reaction in PANI. The integrated self-powered biosensing system enables real-time monitoring of pH, K^+, and glucose with high sensitivity, effectively accommodating varying sweat rates. This work paves the way for the development of stable, high-performance self-powered health monitoring systems, marking a significant advance in personalized healthcare technology.

Supplementary Information The online version contains supplementary material available at https://doi.org/10.1007/s42765-024-00484-8.

Acknowledgements This work was financially supported by the National Natural Science Foundation of China no. T2188101, Gusu's young leading talent (ZXL2021449), Key industry technology innovation project of Suzhou (SYG202108).

Data availability The data that support the findings of this study are available on request from the corresponding author. The data are not publicly available due to privacy or ethical restrictions.

Declarations

Conflict of interest Yuanlong Shao is an editorial board member/editor-in-chief for [Advanced Fiber Materials] and was not involved in the editorial review or the decision to publish this article. All the authors state that there are no conflicts of interest.

References

1. Yin L, Cao M, Kim KN, Lin M, Moon J-M, Sempionatto JR, Yu J, Liu R, Wicker C, Trifonov A, Zhang F, Hu H, Moreto JR, Go J, Xu S, Wang J. A stretchable epidermal sweat sensing platform with an integrated printed battery and electrochromic display. *Nat Electron*. **2022**;*5*:694–705.
2. Chen C, Feng J, Li J, Guo Y, Shi X, Peng H. Functional fiber materials to smart fiber devices. *Chem Rev*. **2023**;*123*:613–62.
3. Lv J, Jeerapan I, Tehrani F, Yin L, Silva-Lopez CA, Jang JH, Joshuia D, Shah R, Liang YY, Xie LY, Soto F, Chen CR, Karshalev E, Kong CC, Yang ZM, Wang J. Sweat-based wearable energy harvesting-storage hybrid textile devices. *Energy Environ Sci*. **2018**;*11*:3431–42.
4. Zhu M, Yu J, Li Z, Ding B. Self-healing fibrous membranes. *Angew Chem Int Edit*. **2022**;*61*: e202208949.
5. Zhu M, Li J, Yu J, Li Z, Ding B. Superstable and intrinsically self-healing fibrous membrane with bionic confined protective structure for breathable electronic skin. *Angew Chem Int Edit*. **2022**;*61*: e202200226.
6. Lv X, Liu Y, Yu J, Li Z, Ding B. Smart fibers for self-powered electronic skins. *Adv Fiber Mater*. **2022**;*5*:401–28.
7. Li J, Cai J, Yu J, Li Z, Ding B. The rising of fiber constructed piezo/triboelectric nanogenerators: From material selections, fabrication techniques to emerging applications. *Adv Funct Mater*. **2023**;*33*:2303249.
8. Libanori A, Chen G, Zhao X, Zhou Y, Chen J. Smart textiles for personalized healthcare. *Nat Electron*. **2022**;*5*:142–56.
9. Yang DS, Ghaffari R, Rogers JA. Sweat as a diagnostic biofluid. *Science*. **2023**;*379*:760–1.
10. Gao M, Wang P, Jiang L, Wang B, Yao Y, Liu S, Chu D, Cheng W, Lu Y. Power generation for wearable systems. *Energy Environ Sci*. **2021**;*14*:2114–57.
11. Song Y, Mukasa D, Zhang H, Gao W. Self-powered wearable biosensors. *Acc Mater Res*. **2021**;*2*:184–97.
12. Qian Z, Yang Y, Wang L, Wang J, Guo Y, Liu Z, Li J, Zhang H, Sun X, Peng H. An implantable fiber biosupercapacitor with high power density by multi-strand twisting functionalized fibers. *Angew Chem Int Edit*. **2023**;*62*: e202303268.
13. Yu Y, Nassar J, Xu C, Min J, Yang Y, Dai A, Doshi R, Huang A, Song Y, Gehlhar R, Ames AD, Gao W. Biofuel-powered soft electronic skin with multiplexed and wireless sensing for human-machine interfaces. *Sci Robot*. **2020**;*5*:eaaz7946.
14. Yin L, Scharf J, Ma J, Doux J-M, Redquest C, Le VL, Yin Y, Ortega J, Wei X, Wang J, Meng YS. High performance printed ago-zn rechargeable battery for flexible electronics. *Joule*. **2021**;*5*:228–48.
15. Bandodkar AJ, Lee SP, Huang I, Li W, Wang S, Su CJ, Jeang WJ, Hang T, Mehta S, Nyberg N, Gutruf P, Choi J, Koo J, Reeder JT, Tseng R, Ghaffari R, Rogers JA. Sweat-activated biocompatible batteries for epidermal electronic and microfluidic systems. *Nat Electron*. **2020**;*3*:554–62.
16. Ju J, Xiao G, Jian Y, Wu L, Sun W, Wang W, Li CM, Qiao Y, Lu Z. Scalable, high-performance, yarn-shaped batteries activated by an ultralow volume of sweat for self-powered sensing textiles. *Nano Energy*. **2023**;*109*: 108304.
17. Xiao G, Ju J, Lu H, Shi XM, Wang X, Wang W, Xia QY, Zhou GD, Sun W, Li CM, Qiao Y, Lu ZS. A weavable and scalable cotton-yarn-based battery activated by human sweat for textile electronics. *Adv Sci*. **2022**;*9*:2103822.
18. Baker CO, Huang X, Nelson W, Kaner RB. Polyaniline nanofibers: broadening applications for conducting polymers. *Chem Soc Rev*. **2017**;*46*:1510–25.
19. Tzou KT, Gregory RV. Improved solution stability and spinnability of concentrated polyaniline solutions using n, n′-dimethyl propylene urea as the spin bath solvent. *Synth Met*. **1995**;*69*:109–12.
20. Mattes BR, Wang HL, Yang D, Zhua YT, Blumenthala WR, Hundleya MF. Formation of conductive polyaniline fibers derived from highly concentrated emeraldine base solutions. *Synth Met*. **1997**;*84*:45–9.
21. Mazzoldi A, Degl'Innocenti C, Michelucci M, De Rossi D. Actuative properties of polyaniline fibers under electrochemical stimulation. *Mat Sci Eng C-Biomim*. **1998**;*6*:65–72.
22. Pomfret SJ, Adams PN, Comfort NP, Monkman AP. Inherently electrically conductive fibers wet spun from a sulfonic acid-doped polyaniline solution. *Adv Mater*. **1998**;*10*:1351–3.
23. Pomfret SJ, Adams PN, Comfort NP, Monkman AP. Electrical and mechanical properties of polyaniline fibres produced by a one-step wet spinning process. *Polymer*. **2000**;*41*:2265–9.

24. Tong X, Sheng G, Yang D, Li S, Lin CW, Zhang W, Chen Z, Wei C, Yang X, Shen F, Shao Y, Wei H, Zhu Y, Sun J, Kaner RB, Shao Y. Crystalline tetra-aniline with chloride interactions towards a biocompatible supercapacitor. *Mater Horiz*. **2022**;*9*:383–92.
25. Yan D, Luo J, Wang S, Han X, Lei X, Jiao K, Wu X, Qian L, Zhang X, Zhao X, Di J, Zhang Z, Gao Z, Zhang J. Carbon nanotube-directed 7 gpa heterocyclic aramid fiber and its application in artificial muscles. *Adv Mater*. **2023**;*36*:2306129.
26. Lee D, Kim SG, Hong S, Madrona C, Oh Y, Park M, Komatsu N, Taylor LW, Chung B, Kim J, Hwang JY, Yu J, Lee DS, Jeong HS, You NH, Kim ND, Kim DY, Lee HS, Lee KH, Kono J, Wehmeyer G, Pasquali M, Vilatela JJ, Ryu S, Ku BC. Ultrahigh strength, modulus, and conductivity of graphitic fibers by macromolecular coalescence. *Sci Adv*. **2022**;*8*:0939.
27. Wang L, Lu J, Li Q, Li L, He E, Jiao Y, Ye T, Zhang Y. A core–sheath sensing yarn-based electrochemical fabric system for powerful sweat capture and stable sensing. *Adv Funct Mater*. **2022**;*32*:2200922.
28. Liu Y, Kumar S. Polymer/carbon nanotube nano composite fibers—a review. *ACS Appl Mater Inter*. **2014**;*6*:6069–87.
29. Xia Z, Li S, Wu G, Shao Y, Yang D, Luo J, Jiao Z, Sun J, Shao Y. Manipulating hierarchical orientation of wet-spun hybrid fibers via rheological engineering for zn-ion fiber batteries. *Adv Mater*. **2022**;*34*:2203905.
30. Jamadade VS, Dhawale DS, Lokhande CD. Studies on electrosynthesized leucoemeraldine, emeraldine and pernigraniline forms of polyaniline films and their supercapacitive behavior. *Synth Met*. **2010**;*160*:955–60.
31. Sainz R, Benito AM, Martínez MT, Galindo JF, Sotres J, Baró AM, Corraze B, Chauvet O, Maser WK. Soluble self-aligned carbon nanotube/polyaniline composites. *Adv Mater*. **2005**;*17*:278–81.
32. Zengin H, Zhou WS, Jin JY, Czerw R, Smith DW, Echegoyen L, Carroll DL, Foulger SH, Ballato J. Carbon nanotube doped polyaniline. *Adv Mater*. **2002**;*14*:1480–3.
33. Cochet M, Maser WK, Benito AM, Callejas MA, Martínez MT, Benoit J-M, Schreiber J, Chauvet O. Synthesis of a new polyaniline/nanotube composite: "In-situ" polymerisation and charge transfer through site-selective interaction. *Chem Commun*. **2001**;*2001*:1450–1.
34. Lv J, Thangavel G, Li Y, Xiong J, Gao D, Ciou J, Tan MWM, Aziz I, Chen S, Chen J, Zhou X, Poh WC, Lee PS. Printable elastomeric electrodes with sweat-enhanced conductivity for wearables. *Sci Adv*. **2021**;*7*:eabg8433.
35. Zhang X, Yang J, Borayek R, Qu H, Nandakumar DK, Zhang Q, Ding J, Tan SC. Super-hygroscopic film for wearables with dual functions of expediting sweat evaporation and energy harvesting. *Nano Energy*. **2020**;*75*: 104873.
36. Chen Y, Xue Y, Liu W, Li S, Wang X, Zhou W, Zhang G, Liu K, Zhang H, Zhao Y, Chen C, Liu Y. Untethered artificial muscles powered by wearable sweat-based energy generator. *Nano Today*. **2023**;*49*: 101765.
37. Liu Y, Huang X, Zhou J, Yiu CK, Song Z, Huang W, Nejad SK, Li H, Wong TH, Yao K, Zhao L, Yoo W, Park W, Li J, Huang Y, Lam HR, Song E, Guo X, Wang Y, Dai Z, Chang L, Li WJ, Xie Z, Yu X. Stretchable sweat-activated battery in skin-integrated electronics for continuous wireless sweat monitoring. *Adv Sci*. **2022**;*9*:2104635.
38. Lv J, Yin L, Chen XH, Jeerapan I, Silva CA, Li Y, Le M, Lin ZH, Wang LW, Trifonov A, Xu S, Cosnier S, Wang J. Wearable biosupercapacitor: harvesting and storing energy from sweat. *Adv Funct Mater*. **2021**;*31*:2102915.
39. Simons P, Schenk SA, Gysel MA, Olbrich LF, Rupp JLM. A ceramic-electrolyte glucose fuel cell for implantable electronics. *Adv Mater*. **2022**;*34*:2109075.
40. Bandodkar AJ, You JM, Kim NH, Gu Y, Kumar R, Mohan AMV, Kurniawan J, Imani S, Nakagawa T, Parish B, Parthasarathy M, Mercier PP, Xu S, Wang J. Soft, stretchable, high power density electronic skin-based biofuel cells for scavenging energy from human sweat. *Energy Environ Sci*. **2017**;*10*:1581–9.
41. Jeerapan I, Sempionatto JR, Pavinatto A, You JM, Wang J. Stretchable biofuel cells as wearable textile-based self-powered sensors. *J Mater Chem A*. **2016**;*4*:18342–53.
42. Wang L, Wang L, Zhang Y, Pan J, Li S, Sun X, Zhang B, Peng H. Weaving sensing fibers into electrochemical fabric for real-time health monitoring. *Adv Funct Mater*. **2018**;*28*:1804456.
43. Mishra AK, Ramaprabhu S. Functionalized graphene-based nanocomposites for supercapacitor application. *J Phys Chem C*. **2011**;*115*:14006–13.
44. Berrada K, Quillard S, Louam G, Lefrant S. Polyanilines and substituted polyanilines: a comparative study of the Raman spectra of leucoemeraldine, emeraldine and pernigraniline. *Synth Met*. **1995**;*69*:201–4.
45. Wang Y, Tran HD, Liao L, Duan X, Kaner RB. Nanoscale morphology, dimensional control, and electrical properties of oligoanilines. *J Am Chem Soc*. **2010**;*132*:10365–73.
46. He X, Fan C, Xu T, Zhang X. Biospired janus silk e-textiles with wet-thermal comfort for highly efficient biofluid monitoring. *Nano Lett*. **2021**;*21*:8880–7.
47. Tong XL, Yang DZ, Hua TJ, Li S, Wang BY, Shao YL. Multifunctional fiber for synchronous bio-sensing and power supply in sweat environment. *Adv Funct Mater*. **2023**;*33*:2301174.
48. Lin H, Yao MY, Tao YF, Li GZ, An L, Li L. A flexible smart monitoring system for the conservation of textile relics. *Adv Funct Mater*. **2021**;*31*:2106088.
49. Tian H, Wang L, Yang W, Li K, Zhang Q, Li Y, Wang H, Hou C. Hierarchical fermat helix-structured electrochemical sensing fibers enable sweat capture and multi-biomarker monitoring. *Mater Horiz*. **2023**;*10*:5192–201.
50. Zhang A, Zhou L, Liang Q, Wang X, Hu X, Jia K, Chu H, Luo Y, Qiu L, Peng H, He S. All-in-one multifunctional and stretchable electrochemical fiber enables health-monitoring textile with trace sweat. *Sci China Mater*. **2023**;*67*:251–60.
51. Li Q, Li D, Lu J, Zou K, Wang L, Jiao Y, Wang M, Gao R, Song J, Li Y, Li F, Ji J, Wang J, Li L, Ye T, He E, Chen H, Wang Y, Ren J, Bai C, Yang S, Zhang Y. Interface-stabilized fiber sensor for real-time monitoring of amniotic fluid during pregnancy. *Adv Mater*. **2023**;*36*:2307726.
52. Wang L, Xie S, Wang Z, Liu F, Yang Y, Tang C, Wu X, Liu P, Li Y, Saiyin H, Zheng S, Sun X, Xu F, Yu H, Peng H. Functionalized helical fibre bundles of carbon nanotubes as electrochemical sensors for long-term *in vivo* monitoring of multiple disease biomarkers. *Nat Biomed Eng*. **2020**;*4*:159–71.
53. Mo L, Ma X, Fan L, Xin JH, Yu H. Weavable, large-scaled, rapid response, long-term stable electrochemical fabric sensor integrated into clothing for monitoring potassium ions in sweat. *Chem Eng J*. **2023**;*454*: 140473.

Publisher's Note Springer Nature remains neutral with regard to jurisdictional claims in published maps and institutional affiliations.

Springer Nature or its licensor (e.g. a society or other partner) holds exclusive rights to this article under a publishing agreement with the author(s) or other rightsholder(s); author self-archiving of the accepted manuscript version of this article is solely governed by the terms of such publishing agreement and applicable law.